PHYSIOLOGY

Biomimetic multifunctional persistent luminescence nanoprobes for long-term near-infrared imaging and therapy of cerebral and cerebellar gliomas

Jianglong Kong[1], Rui Zou[1], Ga-Lai Law[2]*, Yi Wang[1]*

Glioma is the most common malignant primary brain tumor, and the accurate diagnosis of glioma has always been a challenge. Moreover, cerebellar glioma, which is difficult to be detected by magnetic resonance imaging, is not usually diagnosed until after the appearance of clinical symptoms. In this study, TRZD, a near-infrared (NIR) persistent luminescence (PL) nanoparticle with a dual function of imaging and therapy, was synthesized based on $ZnGa_2O_4:Cr^{3+},Sn^{4+}$. TRZD showed excellent rechargeable NIR PL for more than 30 hours in vivo with good tissue penetration for long-term autofluorescence-free imaging. The tumor growth of both the subcutaneous and orthotropic glioma models was significantly inhibited by TRZD. This is the first-time approach using NIR PL nanoprobes for both diagnosis and therapy of glioma. This is also the first-time report of nanotechnology-based diagnosis and therapy of cerebellar gliomas. This study offers a highly promising multifunctional nanoparticle for theranostics of a wide range of brain diseases.

INTRODUCTION

Glioma is one of the most common primary intracranial tumors in the central nervous system (CNS) (*1*). It has the characteristics of poor prognosis, strong invasion, high recurrence rate, and low survival rate (*2*, *3*). Moreover, cerebellar glioma, which accounts for the highest proportion of CNS tumors in children (*4*), is even worse since it is difficult to detect by magnetic resonance imaging and is not usually diagnosed until after the appearance of clinical symptoms (*5*). Tumors in other parts of the brain, such as brain stem gliomas, cerebellopontine angle tumors, fourth ventricle tumors, and pineal area tumors, tend to metastasize to the cerebellum from the surrounding areas. At present, there are many reports on the diagnosis of cerebral gliomas, but there are few literatures on the diagnosis of cerebellar gliomas. Optical imaging has attracted significant attention for diagnosis because of its high sensitivity, relatively low cost of the equipment, and suitability for image-guided surgery. However, its applications were limited by its low spatial resolution and short penetration depth (*6*, *7*). Nanoparticle (NP)–assisted optical imaging system, such as fluorescent silicon NPs (*8*) and quantum dots (QDs) (*9*), have shown improvements. However, the fluorescent nanoprobes need to be excited in real time and are easily interfered by autofluorescence, which limited their applications in clinical trials.

Recently, a previously unknown optical contrast agent, the near-infrared (NIR) persistent luminescence (PL) NP (NIR-PLNP), was reported by de Chermont *et al.* (*10*). This kind of NPs emits NIR PL within the tissue transparency window of 650 to 1350 nm with no background autofluorescence for hours after the termination of excitation (*11*, *12*). Compared with QD and traditional organic dyes, NIR PL has the advantages including the emission of long-term luminescence, multiple excitation bands, and rechargeability. NIR PL has a special nonlinear radiation process that involves the absorption and retention of photons for hours. For biological application, NIR PL has potential to work as previously unknown optical contrast agents for in vivo bioimaging. NIR PL has a high signal-to-noise ratio for bioimaging because most proteins or organelles emit a luminescence signal within the visible or ultraviolet (UV) window (*13*–*17*). Moreover, PL can be renewed; thus, long-term imaging can be performed without the limit of the lifetime of luminescence (*18*). However, although PLNPs provide many advantages, there are still considerable challenges to be overcome before they can be tested in clinical trials.

In the design of drug carriers, consideration of important factors such as biocompatibility, immune-invasive capacity, and protection of the cargoes for long circulation lifetime is necessary due to the different kinds of cell membranes involved for the treatment of different diseases, such as thrombosis (*19*, *20*), ischemic stroke (*21*, *22*), and tumor (*23*, *24*). Surface modification of cell membranes with targeting ligands that specifically bind to tumor cells is likely to further improve the drug delivery efficiency for cancer treatments.

The blood-brain tumor barrier (BBTB), which is between the CNS and peripheral blood circulation, is another challenge in the diagnosis and therapy of glioma (*25*). More than 98% of small-molecule drugs and contrast agents cannot transfer across the BBTB (*26*, *27*). To overcome the BBTB, many drug delivery methods have been developed: (i) The damages caused by the osmotic shocks (*28*), ultrasonic waves (*29*), or magnetic fields (*30*) can temporarily disable the BBTB and allow drugs to transfer from the circulatory system to the CNS. (ii) Cell-penetrating peptides, which conjugate to therapeutic agents and biopolymer drug carriers, are capable of rapidly crossing through the cell membranes of the BBTB (*31*, *32*). (iii) Receptor-mediated BBTB penetration, the most widely used methods, takes advantage of transferrin receptors (TfRs) (*33*), lactoferrin receptors (*34*), folate receptors (*35*), lipoprotein receptor–related protein (*36*), and glucose receptors (*37*).

In this study, a previously unknown NIR-PLNP with the dual function of imaging and therapy was synthesized based on doxorubicin (DOX)– and $ZnGa_2O_4:Cr^{3+},Sn^{4+}$ (ZGOCS)–loaded mesoporous silica NPs [DOX-ZGOCS@MSN (ZD)]. The red blood cell membrane (RBM)

[1]Department of Chemistry, Hong Kong Baptist University, Kowloon Tung, Hong Kong SAR. [2]Department of Applied Biology and Chemical Technology, The Hong Kong Polytechnic University, Hong Hum, Kowloon, Hong Kong SAR.
*Corresponding author. Email: ga-lai.law@polyu.edu.hk (G.-L.L.); yiwang2@hkbu.edu.hk (Y.W.)

was coated on ZD to increase stability and slow down reticulo-endothelial system (RES) uptake, and the T7 peptide for both BBTB penetration and glioma targeting was further conjugated on the surface to form DOX-ZGOCS@MSN@RBM-T7 (TRZD). Such a long lifetime rechargeable nanoprobe could bring high imaging sensitivity and enhanced antitumor efficacy to both the cerebral and cerebellar gliomas. To the best of our knowledge, no such drug delivery approach using the NIR PL nanoprobes for the theranostics of glioma has been reported so far.

RESULTS AND DISCUSSION

Synthesis and physicochemical characterizations of ZGOCS@MSNs, ZGOCS@MSN@RBM, and ZGOCS@MSN@RBM-T7

ZGOCS@MSN@RBM (RZ) was formed by the coating of RBM on ZGOCS@MSNs (ZM), while ZGOCS@MSN@RBM-T7 (TRZ) was synthesized through the surface conjugation of T7 on RZ (Fig. 1). The morphology and size distribution of ZM and RZ were characterized using transmission electron microscopy (TEM) (Fig. 2, A and B). Figure 2A shows that the prepared ZMs were uniform, monodisperse, and spherical NPs. The mesoporous structure and ZGOCS NPs can be clearly observed. These dark spots well distributed in the nanopores of MSNs. Well-dispersed spherical particles with uniform particle sizes were also observed in TEM images of RZ. The size of ZM was 97.25 ± 1.37 nm, while the size of RZ was 115.07 ± 2.75 nm. The cell membrane coating, with an average thickness of 8.91 nm, was successfully formed on the surface of ZM to establish a core-shell structure. To investigate the crystal structure of ZM, x-ray diffraction (XRD) was conducted (Fig. 2C). Compared with the spectrum of $ZnGa_2O_4$ [Joint Committee on Powder Diffraction Standards (JCPDS) no. 38-1240], all the characteristic XRD peaks of ZM matched quite well, which indicated that the pure cubic phase $ZnGa_2O_4$ was obtained. The broad diffraction peak at about 20° was the characteristic signal from the amorphous MSN.

To study the elemental composition of ZM, scanning electron microscopy (SEM) images, elemental mapping images, the spectrum of the energy-dispersive x-ray spectroscopy, and the amounts of representative elements were obtained and calculated, and the results were shown in Fig. 2D and fig. S1. O and Si, which belonged to MSN, and Ga, Zn, Sn, and Cr, which belonged to ZGOCS, were detected, and the amounts were confirmed. PL of ZM was optimized by co-doping Cr^{3+} and Sn^{4+}, since it was reported that the Cr^{3+}/Sn^{4+} co-doped $ZnGa_2O_4$ gave more intense PL than the single Cr^{3+}-doped $ZnGa_2O_4$ (*38*, *39*). Sn^{4+} played an important role in increasing the amount of antisite defects, which were responsible for PL of Cr^{3+} in the $ZnGa_2O_4$ host. These results confirmed that ZM had been successfully produced.

To evaluate the respective stability of ZM, RZ, and TRZ, particle size and size distribution, polydispersity index (PDI), and surface charge of the particles were analyzed using dynamic light scattering. The mean hydrodynamics of ZM, RZ, and TRZ were 181.37 ± 4.01 nm,

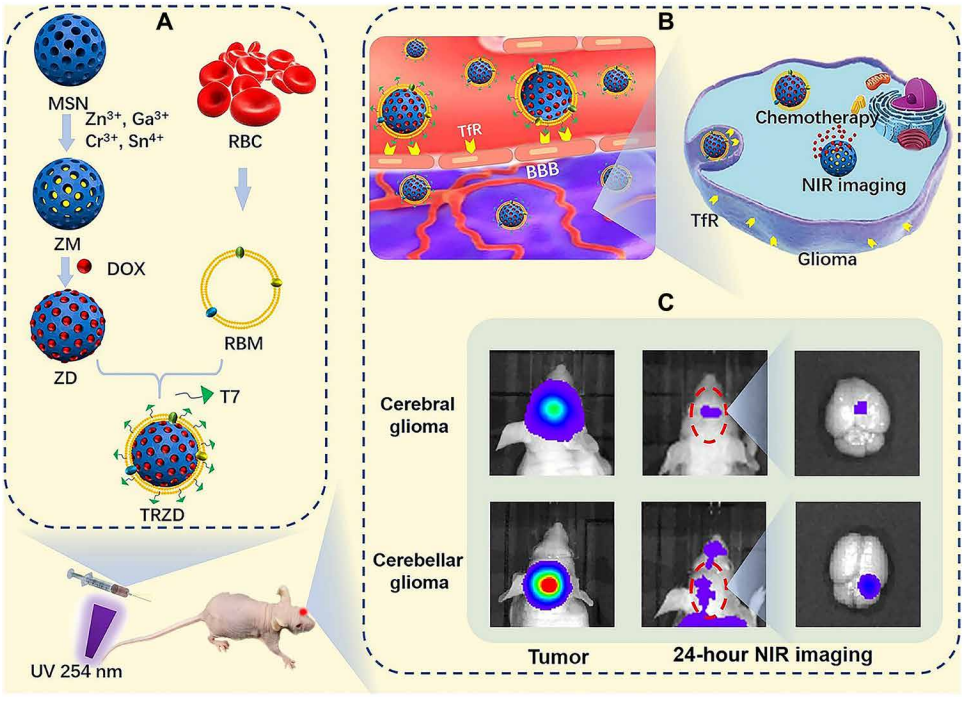

Fig. 1. Scheme of the formation of TRZD and the proposed mechanism of action for the diagnosis and treatment of cerebral and cerebellar gliomas. (**A**) Design of TRZD. ZGOCS was loaded in mesoporous silica NPs (MSNs) to form ZM (ZGOCS@MSN). DOX was loaded in ZM to form ZD. RBM was extracted from red blood cell (RBC) and coated on ZD to form RZD (DOX-ZGOCS@MSN@RBM). T7 peptide, for both BBTB penetration and glioma targeting, was conjugated on RZD to form TRZD (DOX-ZGOCS@MSN@RBM-T7). The suspension of TRZD was excited by 254-nm UV light for 5 min and then injected through the tail vein into the mice. (**B**) Blood-brain barrier (BBB) penetration and glioma targeting of TRZD. In the brain, TRZD penetrates through the BBB via receptor-mediated transcytosis, because T7 exhibits high binding affinity to the TfR, which is overexpressed on BBB. TRZD will also target at glioma cells since TfR is also overexpressed on tumor cells, including glioma cells. After the receptor-mediated endocytosis to glioma cells, DOX will perform a controlled release from TRZD for the chemotherapy of glioma. (**C**) NIR imaging of cerebral and cerebellar gliomas. TRZD, which contains ZGOCS, will show excellent rechargeable NIR PL for more than 30 hours in vivo with good tissue penetration, which enables long-term autofluorescence-free imaging of orthotopic glioma at both cerebrum and cerebellum.

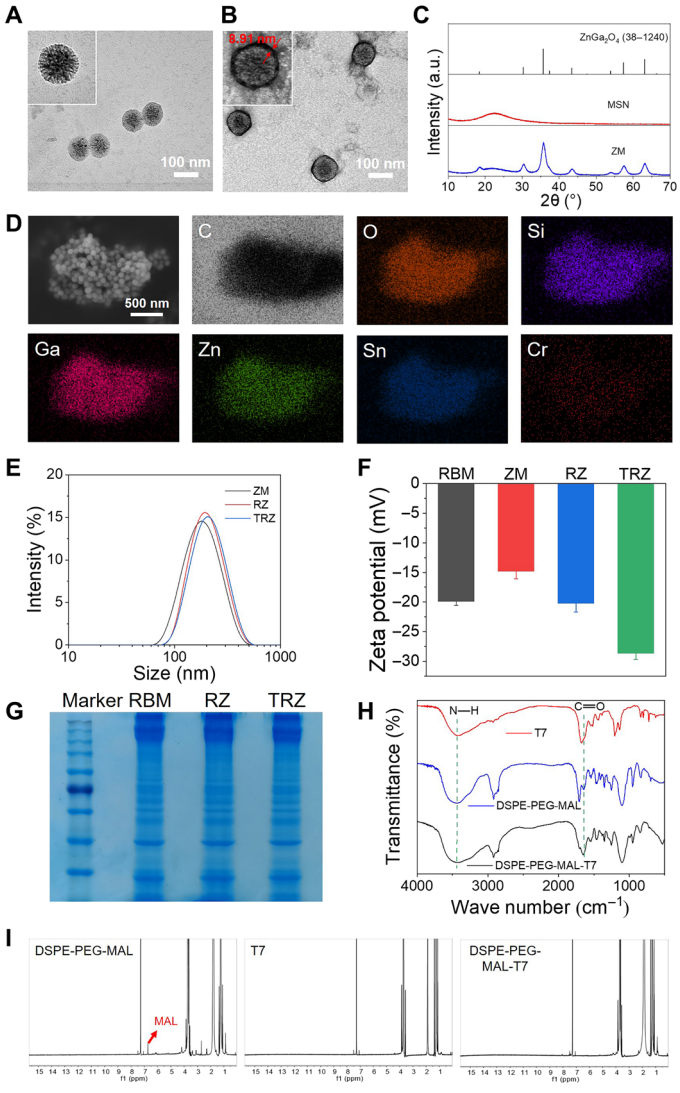

Fig. 2. Structural and chemical characterizations of NPs. TEM images of (**A**) ZM and (**B**) RZ. Scale bars, 100 nm. (**C**) XRD of MSN and ZM. a.u., arbitrary units. (**D**) SEM and elemental mapping images of ZM. Scale bar, 500 nm. (**E**) Size distribution and (**F**) zeta potential of ZM, RZ, and TRZ. (**G**) The respective protein composition of RBM, RZ, and TRZ was examined using SDS-PAGE. (**H**) FTIR and (**I**) ^{1}H NMR spectra of DSPE-PEG-MAL, T7, and DSPE-PEG-MAL-T7.

220.93 ± 0.51 nm, and 205.83 ± 1.50 nm, respectively (Fig. 2E and table S1). With the coating of the cell membrane and the conjugation of the T7 peptides, the size of TRZ was about 25 nm larger than that of ZM. The PDI values of ZM, RZ, and TRZ were 0.17 ± 0.03, 0.11 ± 0.09, and 0.17 ± 0.11, respectively (table S1). The zeta potentials of ZM, RZ, and TRZ were −14.8 ± 1.3 mV, −20.23 ± 1.46 mV, and −28.67 ± 0.97 mV, respectively (Fig. 2F), which indicated that both RZ and TRZ had good stability in the dispersion. The protein composition of the RBM coating on RZ and TRZ was examined using SDS–polyacrylamide gel electrophoresis (PAGE) with Coomassie staining. As shown in Fig. 2G, there was no change in the protein composition of RBM after coating on RZ and TRZ compared to that of RBM itself.

The conjugation between T7 and 1,2-distearoyl-*sn*-glycero-3-phosphoethanolamine-*N*-[maleimide(polyethylene glycol)] (DSPE-PEG-MAL) was studied using Fourier transform infrared (FTIR) and ^{1}H nuclear magnetic resonance (NMR). Figure 2H shows the fingerprints of DSPE-PEG-MAL in the spectrum at 3466.96 and 1657.54 cm^{-1}, which were attributed to the weak stretching vibration of N—H and C=O, respectively. These two stretching bands are characteristic absorptions of amide II in the structure of DSPE-PEG-MAL. In the spectrum of DSPE-PEG-MAL-T7, the intensity of the two peaks at 3466.96 and 1657.54 cm^{-1} increased significantly compared with those in the spectrum of DSPE-PEG-MAL, which could be attributed to the sum of the seven amide II in the T7 structure. The ^{1}H NMR spectra of DSPE-PEG-MAL, T7, and DSPE-PEG-MAL-T7 were shown in Fig. 2I. The peak at 6.73 parts per million (ppm) indicated MAL. After the conjugation of T7 and DSPE-PEG-MAL to form DSPE-PEG-MAL-T7, the peak at 6.73 ppm disappeared. All of these results confirmed the successful conjugation of DSPE-PEG-MAL and T7. The preparations with different ratios of ZM and the tetramethylrhodamine (TMR)–labeled DSPE-PEG-MAL-T7 showed different conjugation rates between T7 and ZM (fig. S2). When the ratio was 10:1, the conjugation rate reached 97.42 ± 0.18%. Therefore, the ratio 10:1 of T7 and ZM was selected for further experiments.

NIR PL imaging of TRZ

PL excitation and emission spectra of the aqueous dispersion of ZM were obtained at 240 and 695 nm, respectively (Fig. 3A). The decay curve and the average lifetime of PL of ZM were recorded and calculated (fig. S3). Figure 3B shows that ZM could be repeatedly reactivated using 254-nm UV light without obvious loss of the intensity of PL. After excitation using 254-nm UV light for 5 min at room temperature, PL intensity was significantly enhanced (Fig. 3C). After the coating of RBM on ZM to form RZ, there were no changes in PL intensity between ZM and RZ (Fig. 3D). RZ had an afterglow time of over 2 hours at the excitation wavelength of 254 nm. PL of RZ could be renewed by UV light (Fig. 3E). The tissue penetration depth study of PL of TRZ was conducted (fig. S4), and the penetration depth of the excitation light (254 nm) was also evaluated (fig. S5). After the injection of RZ via tail vein, the imaging of PL in the normal mouse model was recorded using the charge-coupled device camera of an in vivo imaging system. The results confirmed that ZM, RZ, and TRZ could all be used as imaging probes for diagnosis purposes (fig. S6). The long-lasting and renewable luminescence of TRZ ensured long-term body imaging without being limited by luminescence duration and autofluorescence.

Drug loading and biosafety of ZM, RZ, and TRZ

The successful encapsulation of DOX in ZD, RZD (DOX-ZGOCS@MSN@RBM), and TRZD was studied using UV-visible spectroscopy, and the spectra were shown in Fig. 4A. The peak at 410 nm corresponded to RBM in both RZD and TRZD. The broad peak at 480 nm corresponded to DOX. The in vitro release of DOX from DOX, ZD, RZD, and TRZD was studied. Our result showed that free DOX had a burst release at the start of the test, and the release in phosphate-buffered saline (PBS) reached 100% after about 2 hours. ZD, RZD, and TRZD showed controlled release of DOX, and both RZD and TRZD had a slower release rate than ZD (Fig. 4B). In addition, the respective release of RZD and TRZD in the solvents of PBS with 10% serum (pH 7.4) (Fig. 4C) and cerebrospinal fluid (CSF) (Fig. 4D) also showed a slower release rate than that of ZD. These results confirmed the enhanced stability of ZM and the controlled release behavior of ZD, RZD, and TRZD after the red blood cell (RBC) membrane coating. Encapsulation efficiency

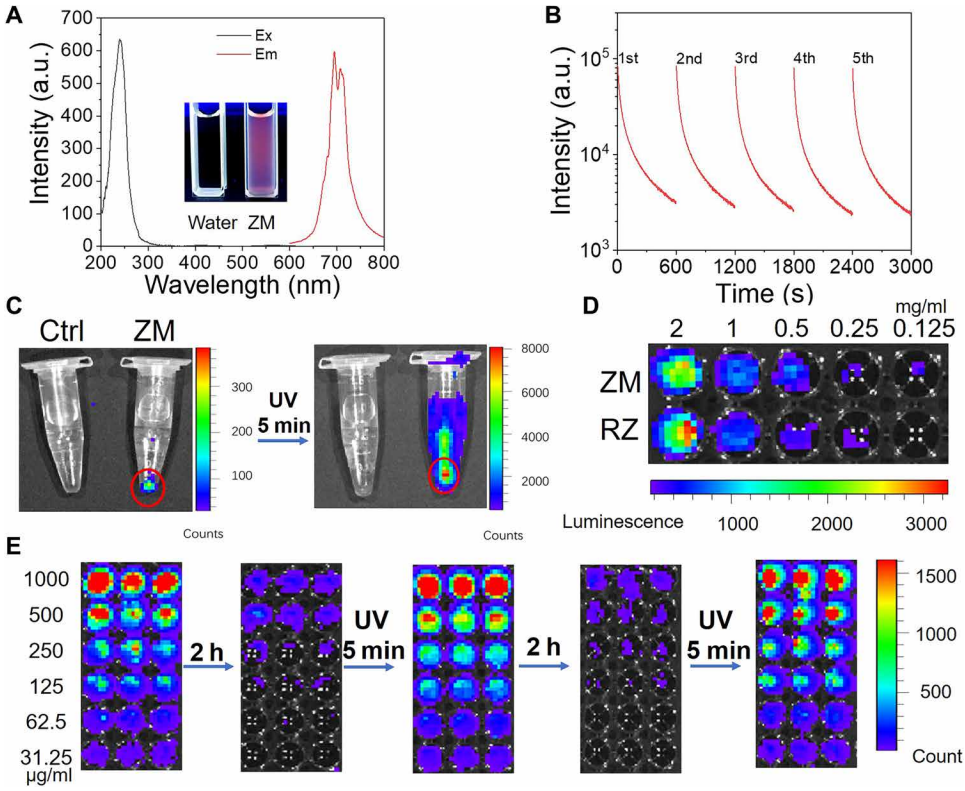

Fig. 3. Evaluations of the persistent luminescence of NPs. (**A**) Excitation (Ex) and emission (Em) spectra of the aqueous dispersion of ZM. The inset shows a digital photo of the aqueous dispersion of ZM under 254-nm UV light, where the deionized water was set as control. (**B**) Renewable PL of ZM. (**C**) PL of ZM before and after UV excitation. (**D**) PL of ZM and RZ after UV excitation. (**E**) Renewed PL of various concentrations of RZ after 5-min excitation using UV light.

(EE) and loading efficiency (LE) of ZD at various DOX to ZM ratios were obtained (table S2). ZD with a DOX to ZM ratio of 1:8 showed the highest EE and LE of 97.54 ± 0.17% and 10.87 ± 0.02%, respectively, and was chosen for further study. The high EE and LE confirmed that ZM was a good drug carrier of DOX.

Before the in vivo evaluations of NPs, the study of the hemolytic assay of NPs was conducted to confirm the safety of NPs. ZM, RZ, and TRZ were separately incubated with the blood collected from the mice for 2 hours at 37°C. Water and PBS were selected as positive and negative controls, respectively. Figure S7 showed that the deionized (DI) water group caused hemolysis, while no obvious hemolysis was observed in the PBS, ZM, RZ, or TRZ group. Furthermore, the effect of the concentrations of TRZD on hemolysis was studied and the result was shown in Fig. 4E. The hemolytic rate was slightly increased with increased concentration of TRZD. The hemolytic rate was still at a low level even at a high concentration of 500 μg/ml, indicating good biocompatibility of TRZD.

Blood chemistry test was then conducted (Fig. 4, F to H, and fig. S8). The alanine aminotransferase (ALT) and aspartate aminotransferase (AST) levels are related to the functions of the liver. Increased levels of ALT and AST are usually caused by liver damage or disease. The creatinine (CREA) levels and blood urea nitrogen (BUN) levels are related to the functions of the kidney. Elevated CREA and BUN levels indicate impaired kidney function or kidney disease. The AST levels of mice treated with DOX were significantly higher than those of the PBS groups (Fig. 4F). BUN levels of mice treated with ZM or RZD were significantly lower than those of the PBS group (Fig. 4G). In addition, RZD caused a significant increase in CREA levels (Fig. 4H). No significant hematological toxicity was caused by TRZD, which confirmed the lower toxicity and better in vivo safety of TRZD than the other NPs. The advantage of TRZD in biosafety could be due to the integrated effect of the enhanced targeting ability of T7 conjugation, the minimized RES uptake because of membrane coating, and the controlled drug release of DOX from ZM.

The short blood circulation time of the drug is a challenge to drug delivery in chemotherapy. We compared the pharmacokinetic profiles of DOX, ZD, RZD, and TRZD (Fig. 4I). The elimination half-life ($T_{1/2}$) of RZD (18.2 hours) and TRZD (17.4 hours) was higher than that of ZD (6.6 hours) and DOX (1.7 hours). The enhanced blood retention of the drug indicated that RBM coating could make RZD and TRZD invisible to the host immune system.

Cellular uptake and permeability through the in vitro blood-brain tumor barrier

The cytotoxicity of DOX, ZM, ZD, RZD, and TRZD on U87-MG cells was evaluated using the traditional Cell Counting Kit-8 (CCK-8) method. After a 48-hour incubation of NPs and cells, ZM showed negligible cytotoxicity at concentrations of 0.5, 1, 5, and 10 μg/ml in U87-MG cells, indicating good biocompatibility of ZM (Fig. 5A). Figure 5B shows that ZD displayed lower cytotoxicity than free DOX, which could be due to the sustained release of DOX from ZM. The free DOX and TRZD exhibited the strongest cellular toxicity at DOX equivalent concentrations of 0.5, 1, and 5 μg/ml, while the coating of the RBC membrane reduced the toxicity of

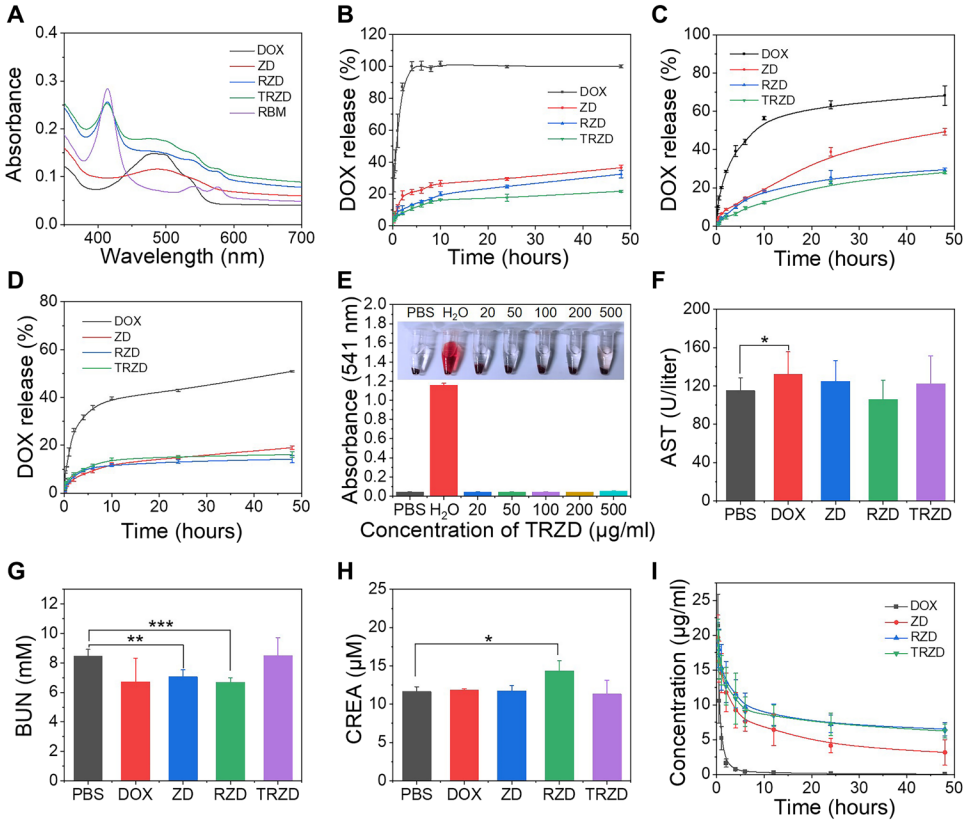

Fig. 4. Evaluations of the controlled release and biosafety of DOX-loaded NPs. (**A**) UV-visible spectra of DOX, ZD, RZD, and TRZD. Cumulative releases of DOX from DOX, ZD, RZD, and TRZD in (**B**) PBS (pH 7.4), (**C**) PBS with 10% serum (pH 7.4), and (**D**) cerebrospinal fluid (pH 7.2) at 37°C. Data are presented as means ± SD ($n = 3$). (**E**) Hemolysis test of TRZD using mouse blood at 37°C for 2 hours ($n = 3$). Deionized water and PBS were selected as positive and negative controls, respectively. (**F** to **H**) Blood chemistry tests: (F) aspartate aminotransferase (AST), (G) blood urea nitrogen (BUN), and (H) creatinine (CREA). Data are presented as means ± SD ($n = 5$); $^{***}P < 0.001$, $^{**}P < 0.01$, and $^{*}P < 0.05$. (**I**) In vivo pharmacokinetic profiles after intravenous injections of DOX, ZD, RZD, and TRZD. Data are presented as means ± SD ($n = 3$).

RZD. This indicated that the function of T7 on the TRZD surface enhanced the targeting abilities of NPs to U87-MG cells and thereby increased the cytotoxicity to the cells compared to that of RZD. DOX, ZD, RZD, and TRZD at a DOX equivalent concentration of 5 μg/ml were incubated with U87-MG cells for 24 hours, and the induced apoptosis was measured using the Annexin V-FITC Apoptosis Detection Kit. As shown in Fig. 5 (D and E), the apoptotic ratios of the cells were 22.26 ± 1.05% and 22.02 ± 2.64% after treatments of free DOX and ZD, respectively. However, U87-MG cells incubated with RZD and TRZD showed higher levels of apoptosis of 24.26 ± 0.54% and 27.80 ± 1.60%, respectively. Figure 5E shows that TRZD significantly increased the rate of apoptosis, which confirmed that the T7 peptide on the surface of TRZD enhanced the uptake of TRZD by cells, and thereby induced more cell apoptosis.

The cellular uptake of DOX, ZD, RZD, and TRZD by U87-MG cells was studied (Fig. 5F). U87-MG cells were cultivated with DOX, ZD, RZD, or TRZD at a DOX equivalent concentration of 2 μg/ml for 1 hour. DAPI (4′,6-diamidino-2-phenylindole), which gave blue fluorescence, was used to stain the nucleus, and the red fluorescence was given by DOX. Comparison of the cellular uptake of DOX, ZD, RZD, and TRZD showed that the intensity of the red fluorescence in the TRZD group increased substantially, which indicated the enhancement in the cellular uptake of TRZD by the conjugation of the T7 peptide.

Flow cytometry was used to quantify the fluorescence intensity in the cells after the cellular uptake of NPs (Fig. 5C), and the results of the statistical analysis were shown in Fig. 5G. It could be seen that TRZD showed enhanced cellular uptake, and the fluorescence given by TRZD had significant differences to that given by ZD and RZD. This further suggested that the conjugation of T7 peptide could efficiently promote the cellular uptake of U87-MG. To study the permeability of NPs through the blood-brain barrier (BBB)/BBTB, a monolayer of the endothelial bEnd.3 cells was established and used as an in vitro BBB/BBTB model (Fig. 5H). The cell monolayer was integrated and ready for use when the transepithelial electrical resistance (TEER) value was ≥180 ohm·cm^2. ZM, RZ, and TRZ were separately added to the apical chamber of the Transwell. The results showed that, after 4 hours of incubation with TRZ, luminescence intensities in the apical chamber and basolateral chamber were significantly higher than those after the incubation with ZM and RZ, respectively (Fig. 5, I, K, and L). As shown in Fig. 5J, the TEER value of each group did not show any significant changes throughout the experiment, suggesting that the integrity of the bEnd.3 cell monolayer was maintained (*40*). The in vitro BBB/BBTB study concluded that T7 could efficiently promote the penetration of TRZ through the BBB/BBTB following TfR receptor–mediated transcytosis (*41*).

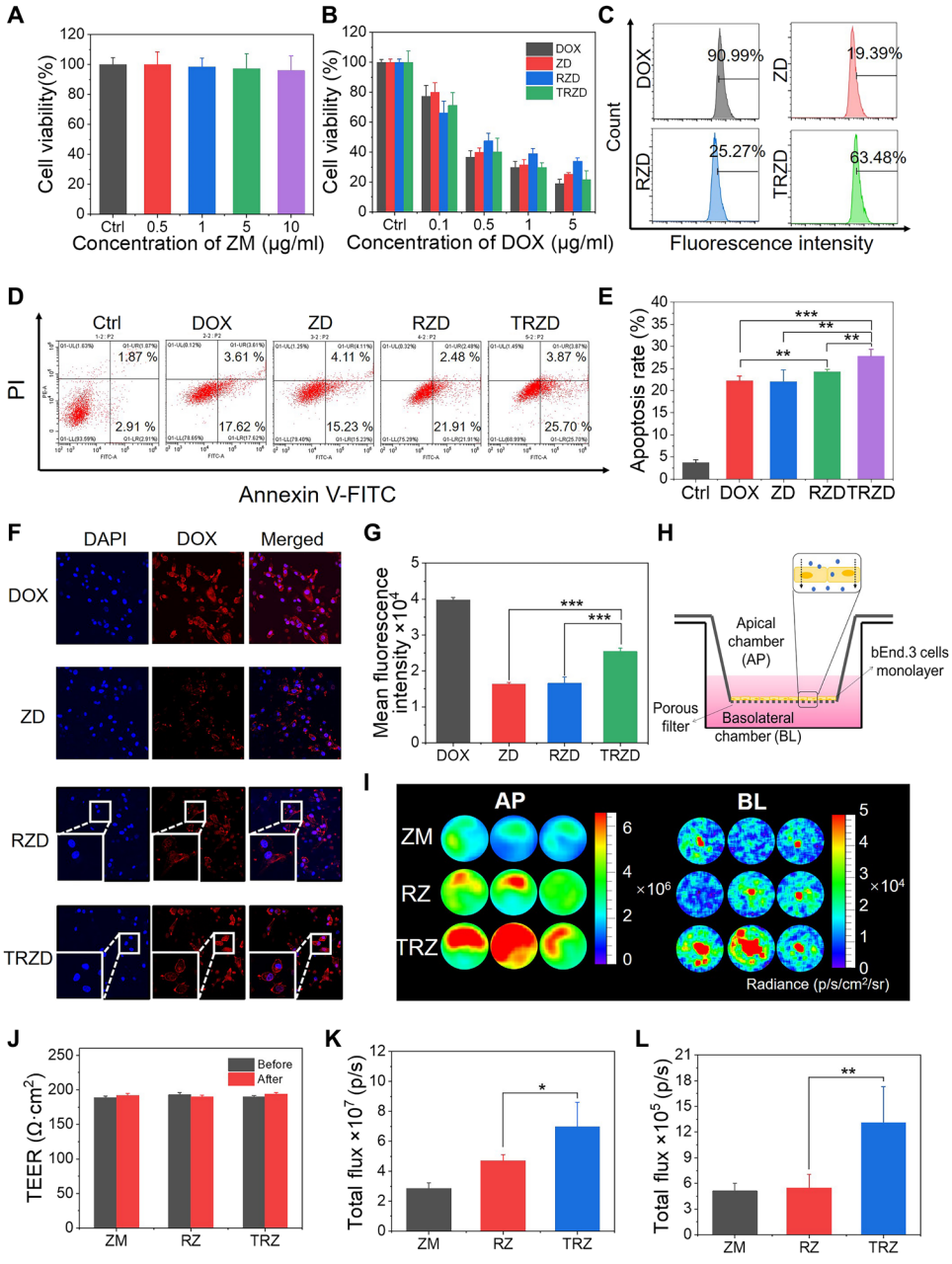

Fig. 5. In vitro studies of cytotoxicity, cellular uptake, and BBB penetration of DOX-loaded NPs. (**A**) Cell viability of U87-MG cells incubated with various concentrations of ZM ($n = 6$). (**B**) Cell viability of U87-MG cells incubated with various concentrations of DOX, ZD, RZD, and TRZD ($n = 6$). (**C**) Histogram profiles of flow cytometry of U87-MG cells incubated with DOX, ZD, RZD, and TRZD for 2 hours ($n = 3$). (**D**) Apoptotic effect of DOX on U87-MG cells. (**E**) Fluorescence intensities of apoptotic cells analyzed by flow cytometry and annexin V–fluorescein isothiocyanate (FITC)/propidium iodide (PI) double staining. Data are presented as means ± SD ($n = 3$); $^{**}P < 0.01$, $^{***}P < 0.001$. (**F**) Confocal laser scanning microscopy images of U87-MG cells treated with DOX, ZD, RZD, and TRZD for 2 hours. Blue fluorescence showed the cell nucleus, while red fluorescence indicated NPs. (**G**) Statistical results of fluorescence intensities of flow cytometry tests. Data are presented as means ± SD ($n = 3$); $^{***}P < 0.001$. (**H**) Scheme of the setup of the Transwell for in vitro BBB/BBTB penetration experiments. (**I**) Luminescence images of the apical (AP) chamber and the basolateral (BL) chamber of the Transwell after 4 hours of incubation with ZM, RZ, and TRZ. (**J**) Transepithelial electrical resistance (TEER) of the bEnd.3 monolayer measured before and after incubation with ZM, RZ, and TRZ. Data are presented as means ± SD ($n = 3$). Luminescence intensities of (**K**) AP and (**L**) BL. Data are presented as means ± SD; $^{*}P < 0.05$ and $^{**}P < 0.01$.

In vivo luminescence imaging and biodistribution study using the subcutaneous U87 tumor model and orthotopic cerebral/cerebellar glioma models

To evaluate the capability of TRZ as the optical probe for biomedical imaging, in vivo luminescence imaging using a subcutaneous U87 tumor model was conducted. In Fig. 6A, the tumors in the mouse model were marked using the red circle. After excitation using the 254-nm UV light for 5 min, the suspension (100 μl, 2 mg/ml) of TRZ was injected into the mouse model through the tail vein. Thirty minutes after the injection, PL at the tumor site of the mice could be observed without in situ excitation, indicating that a certain amount of TRZ was transported to and accumulated at the tumor (Fig. 6A).

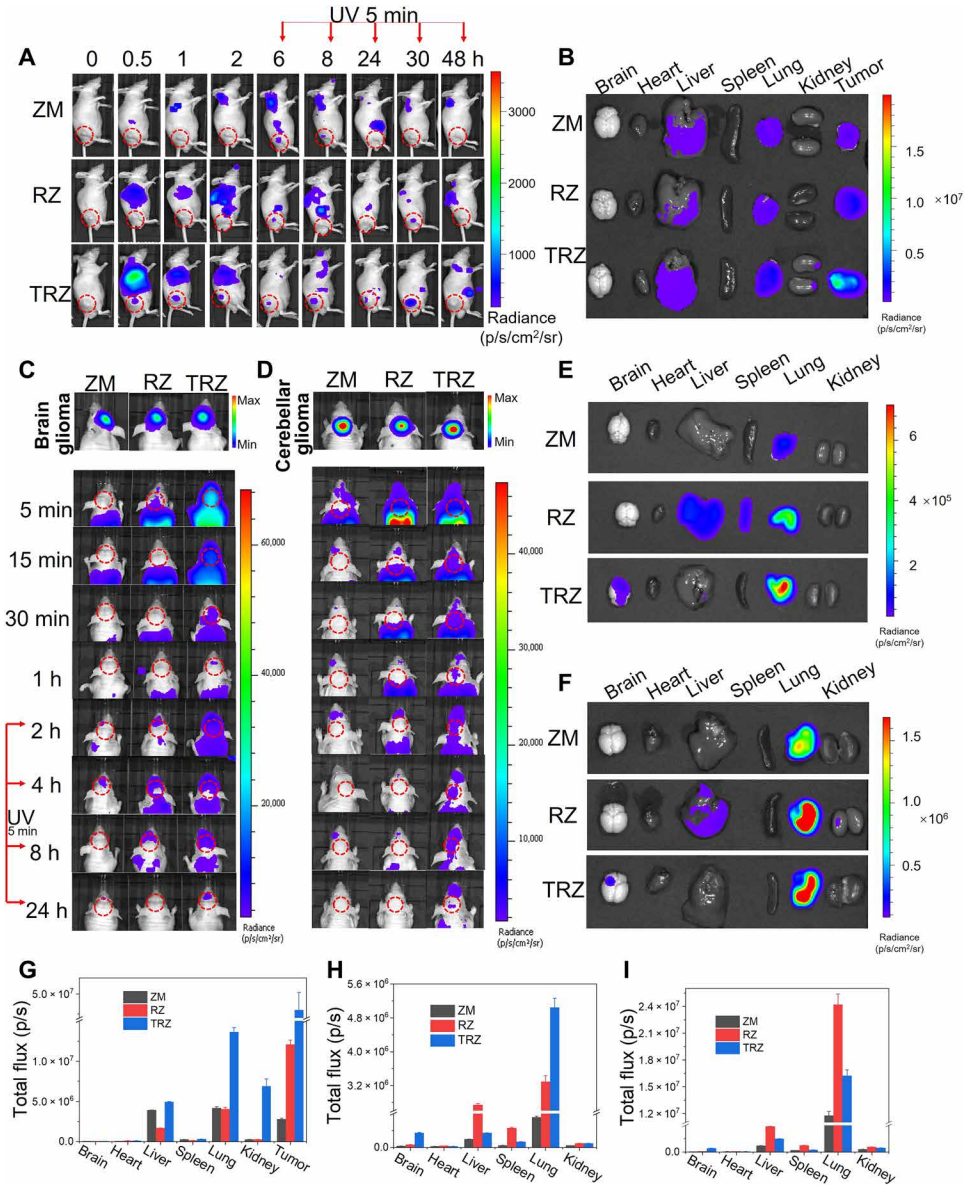

Fig. 6. In vivo NIR persistent luminescence images of the subcutaneous tumor model and orthotopic cerebral/cerebellar glioma model. (**A**) In vivo imaging of the subcutaneous tumor treated with ZM, RZ, and TRZ at various time points and (**B**) ex vivo imaging of major organs as well as the tumor. In vivo imaging of orthotopic (**C**) cerebral and (**D**) cerebellar brain glioma mice at various time points with treatments of ZM, RZ, and TRZ. Ex vivo imaging of major organs as well as the tumor of the (**E**) cerebral and (**F**) cerebellar glioma model after 1-hour treatment of ZM, RZ, and TRZ. Luminescence intensities of major organs as well as the tumor of the (**G**) subcutaneous tumor model, and (**H**) orthotopic cerebral and (**I**) cerebellar glioma models after treatment for an hour ($n = 3$).

To evaluate the in vivo rechargeability of TRZ, the tumor region was irradiated with 254-nm UV light for 5 min at the time points of 2, 6, 8, 24, and 30 hours. The NIR PL of TRZ could be observed again after each in situ excitation. Benefiting from its rechargeability, the application of TRZ as a NIR PL probe was no longer limited by the decay behavior of the traditional PL probes. At the time points of 1, 2, 6, 8, 24, and 30 hours, similar luminescence signals were observed at the tumor site of the TRZ group, while the ZM and RZ groups generally did not show the distinct luminescence signal at the tumor site for almost all the time points, except for the time points of 6 and 8 hours for the ZM group and those of 6 and 30 hours for the RZ group. In summary, it was demonstrated that TRZ was capable of long-time in vivo imaging assisted by the repeat in situ excitation of UV light.

The relative long-term biodistribution of TRZ in the tumor mouse model was studied by ex vivo NIR luminescence imaging. Major organs were collected from the mouse model at 24 hours after the intravenous injection of TRZ. The NIR luminescence images of major organs as well as the tumor were obtained (Fig. 6B), and luminescence intensities were calculated and shown in Fig. 6G. The NIR luminescence signal could be detected in the organs. The highest intensity of luminescence was observed in the tumor of the TRZ group, which confirmed that TRZ had an enhanced targeting ability to glioma by T7 as well as a minimized RES uptake because of the

cell membrane coating. The brain sections were also obtained and observed using a confocal microscope (fig. S9). DAPI was used to dye the nuclei, and fluorescein isothiocyanate (FITC) was used to show the cells. The results showed that TRZ (red fluorescence) entered glioma cells and stayed around the nuclei. The targeting effect and the prolonged circulation suggested that TRZ had a high potential as nanoprobes for imaging and therapy with targeting drug delivery.

To evaluate the performance of TRZ for the diagnosis of orthotopic glioma, mouse models of orthotopic brain glioma at the regions of cerebrum (Fig. 6C) and cerebellum (Fig. 6D) were established and tested. After 10 days of inoculation of U87-Luc cells in the brain, the tumor size, which was marked by the red circle, was recorded using IVIS Spectrum Live Imaging System (IVIS) (Fig. 6, C and D). Then, NPs were intravenously injected into orthotopic glioma-bearing mice, and luminescence images at various time points of 5, 15, 30, and 60 min were captured. The luminescence images were also taken at the time points of 2, 4, 8, and 24 hours after the renewal of PL using UV light for 5 min. At 1 and 24 hours, the luminescence of TRZ was shown at the tumor sites, while the mice in the groups of ZM and RZ showed no luminescence at the tumor site. TRZ with the high targeting ability and immune escape characteristics was able to penetrate the BBTB and bind to U87-MG cells at the tumor site. The ex vivo images of major organs as well as the tumor showed a clear luminescence signal in the brain tumor region (Fig. 6, E and F), an observation that was consistent with the results of the in vivo studies mentioned above. These results confirmed that TRZ was capable of tumor targeting PL imaging for the diagnosis of glioma.

The clearance of NPs from the brain and the body was studied. After the administration of ZM, RZ, and TRZ, orthotopic glioma model mice were sacrificed at 24 and 48 hours. The brains were obtained, and the brain tissue slices were prepared and observed using IVIS (fig. S10). The results showed that, 24 hours after administration, RZ and TRZ were observed and accumulated in the tumor, while ZM could not be observed in the brain. Forty-eight hours after administration, no luminescence of ZM, RZ, and TRZ could be observed in the brain. The luminescence intensity of the RZ and TRZ groups decreased 1.5- and 2-fold, respectively, from 24 to 48 hours after the administration. The results indicated that ZM, RZ, and TRZ were capable to leave the brain to avoid potential long-time disturbance.

We also studied the possibility of the release of the metal ions from NPs, and the results were shown in fig. S11. One milligram of ZM was dissolved using the mixed solvent in the ratio of HF:HNO_3:HCl = 1:1:1, and the original total content of Cr^{3+} and Sn^{4+} loaded in ZM was determined by inductively coupled plasma mass spectrometry (ICP-MS). The results showed that the concentrations of Cr^{3+} and Sn^{4+} in ZM were 66.03 ± 1.78 and 184.58 ± 2.53 parts per billion (ppb), respectively. Then, 1 mg of ZM was placed in dialysis bags and dialysis was carried out in the solution of PBS (pH 7.4), fetal bovine serum (FBS) (pH 7.4), and CSF (pH 7.2). After 7 days, the sample solution outside the dialysis bag was collected and the content of elements in the solution was measured using ICP-MS. The results showed that the concentrations of Cr^{3+} and Sn^{4+} were 1.82 ± 0.07 and 1.03 ± 0.29 ppb in PBS, 3.97 ± 1.19 and 12.7 ± 1.22 ppb in FBS, and 4.20 ± 0.52 and 9.10 ± 0.22 ppb in CSF (fig. S10). Less than 10% of Cr^{3+} and Sn^{4+} will be released after 7-day soaking in PBS, FBS, and CSF. While 24 hours after administration, NPs started to leave the brain and about half of TRZ was left after 48 hours (fig. S9). Therefore, Cr^{3+} and Sn^{4+} in ZM will not be released from the inorganic core and will leave the brain starting from 24 hours after administration.

Figure 6 (E and F) also shows that a large quantity of TRZ was accumulated in the lungs. After the injection of NP suspensions in mice via their tail veins, TRZ entered the heart following blood circulation. As a biomimetic NP coated with RBM, TRZ then entered the lung through the pulmonary artery, where the real erythrocyte completed the exchange of carbon dioxide and oxygen. TRZ then returned to the heart through the pulmonary vein. In the pulmonary artery, TRZ was filtered and intercepted by the lung tissue, which may delay the returning of TRZ to the heart, and thus, the accumulation of a large quantity of TRZ in the lungs was observed.

Evaluation of the antitumor activity using a subcutaneous U87 tumor model

The timeline of the experiment was shown in Fig. 7A. Briefly, nude mouse models with subcutaneous glioma were divided into five groups (n = 10), which were given treatments of PBS, DOX, ZD, RZD, and TRZD. As shown in Fig. 7 (B and C) and fig. S12, 16 days after the first treatment, the tumor volume of mice in the TRZD group was the smallest among the five groups. As shown in Fig. 7D, the average weight of all groups showed an upward trend through the duration of the study. The survival time of the group treated by PBS was less than 60 days, while the TRZD group achieved the longest survival (Fig. 7E). The antitumor effect of TRZD was further studied using terminal deoxynucleotidyl transferase–mediated deoxyuridine triphosphate nick end labeling (TUNEL) and CD31 staining of the excised tumor tissues. After TUNEL staining (Fig. 7F), more intense green fluorescence indicated higher degrees of apoptosis. After CD31 staining (Fig. 7G), less red fluorescence indicated higher degree of tumor inhibition. The TRZD group showed the maximum degree of apoptosis and minimum degree of angiogenesis, which indicated that TRZD performed the best in the suppression of the growth of the tumor cells among the treatment groups. Histopathological analysis of the tissues of major organs was also conducted (fig. S13). In the groups of DOX and ZD, the arrangement of myocardial cells was disordered, and some myocardial fibers in the heart were broken (labeled by A and marked by the red arrows). There was no such damage shown in the RZD or TRZD groups, which was probably due to the reduced DOX accumulation in the heart. Owing to the cell membrane coating on RZD and TRZD, the cardiotoxicity of DOX was reduced. In addition, in the groups of DOX and RZD, the boundary of some glomeruli was not clear, and inflammatory cell infiltration and renal tubular stenosis were also found in the kidney (labeled by B and marked by the red arrows). The results confirmed that, as a brain-targeting drug carrier, TRZD had no safety problems and no side effects on major organs.

Evaluation of the antitumor activity using a cerebral orthotropic U87 glioma model

The chemotherapeutic efficacy of TRZD was evaluated using a cerebral orthotropic U87 tumor-bearing mouse model (Fig. 8A). Five groups of mice (n = 6) were intravenously injected with 200-μl suspensions of PBS, DOX, ZD, RZD, and TRZD, every 3 days. From the results of the change of body weight (Fig. 8B), it can be concluded that the weight of mice in all the groups decreased through the duration of the experiments with no significant difference, and the

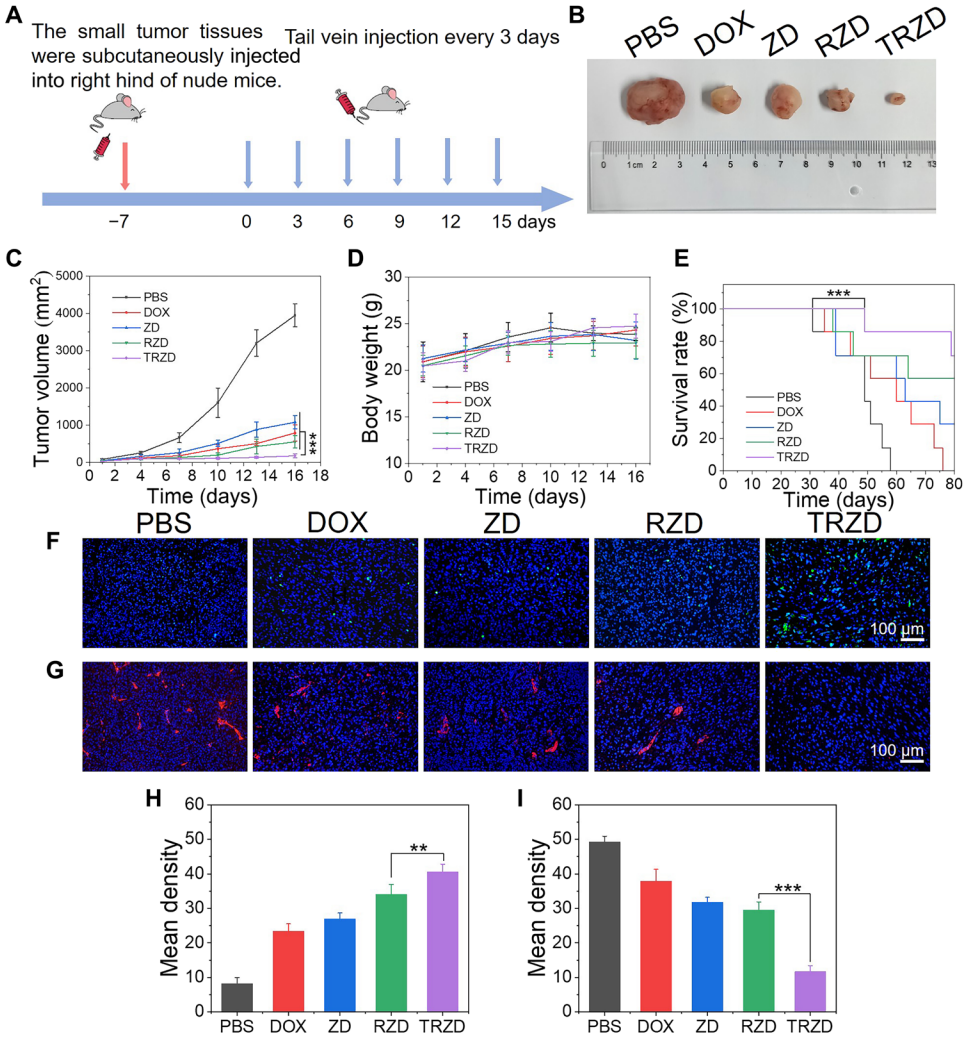

Fig. 7. In vivo study of the antitumor efficacy using a subcutaneous glioma model. Mice were administered with PBS, DOX, ZD, RZD, or TRZD after tumor implantation. (**A**) Scheme of the experimental timeline. (**B**) Representative tumor images of mice in different groups. (**C**) Volume of the tumors of the subcutaneous glioma mouse model of the PBS, DOX, ZD, RZD, and TRZD groups. Tumor volumes were measured every 3 days after the first administration of PBS, DOX, ZD, RZD, and TRZD. Data are presented as means ± SD ($n = 10$). (**D**) Profiles of the change of the body weight of the mice. Data are presented as means ± SD ($n = 10$). (**E**) Cumulative survival study. (**F**) TUNEL staining and (**G**) CD31 staining of tumor tissues of the subcutaneous glioma model. Cell nuclei were stained with DAPI (blue). The mean fluorescence intensity of the images of (**H**) TUNEL staining and (**I**) CD31 staining was calculated using ImageJ. Data are presented as means ± SD ($n = 5$); $^{***}P < 0.001$ and $^{**}P < 0.01$.

PBS group decreased the most. The tumor size and the intensities of the fluorescence given by the tumor cells were recorded and calculated. As shown in Fig. 8 (C and D), fluorescence intensities at the glioma site, which were indicative of the tumor size, of the TRZD group were lower than those of the other groups at all the time points, which indicated the highest level of suppression of the glioma growth of the TRZD group. It was also shown that the mice in the TRZD group survived the longest time among all groups (Fig. 8E).

The images of the hematoxylin and eosin (H&E) staining of the slices of brain tissues were also obtained (Fig. 8F). The tumor region was marked by a yellow dashed line. The TRZD group showed the smallest tumor size as compared with the other groups after the 15-day treatment. These results were consistent with the in vivo images (Fig. 8, C and D), demonstrating that TRZD could significantly inhibit the growth of glioma. The images of TUNEL staining of the TRZD group showed an extensive cell apoptosis in the glioma region, but not in the normal brain tissue, confirming the good selectivity of TRZD (Fig. 8, G and I). The images of CD31 staining showed that the expression of CD31 decreased in the group of PBS, to that of DOX, ZD, RZD, and TRZD, and the intensity of the red fluorescence of TRZD group was significantly lower than those of the other groups (Fig. 8, H and J). This indicated that TRZD could induce ablation of blood vessels in glioma and cause apoptosis of glioma cells the most among the groups. As shown in the images of the H&E staining of major organs (fig. S14), DOX caused the rupture of some myofibrils and showed strong cardiotoxicity in the heart (labeled by A and marked by the white arrow). ZD causes the thickening of the alveolar septum and the infiltration of the inflammatory cells in the lung (labeled by B and marked by the white arrow). In addition, DOX and ZD caused the infiltration of the renal interstitial inflammatory cells, such as macrophages and lymphocytes, and the unclear boundary of glomeruli in the kidney

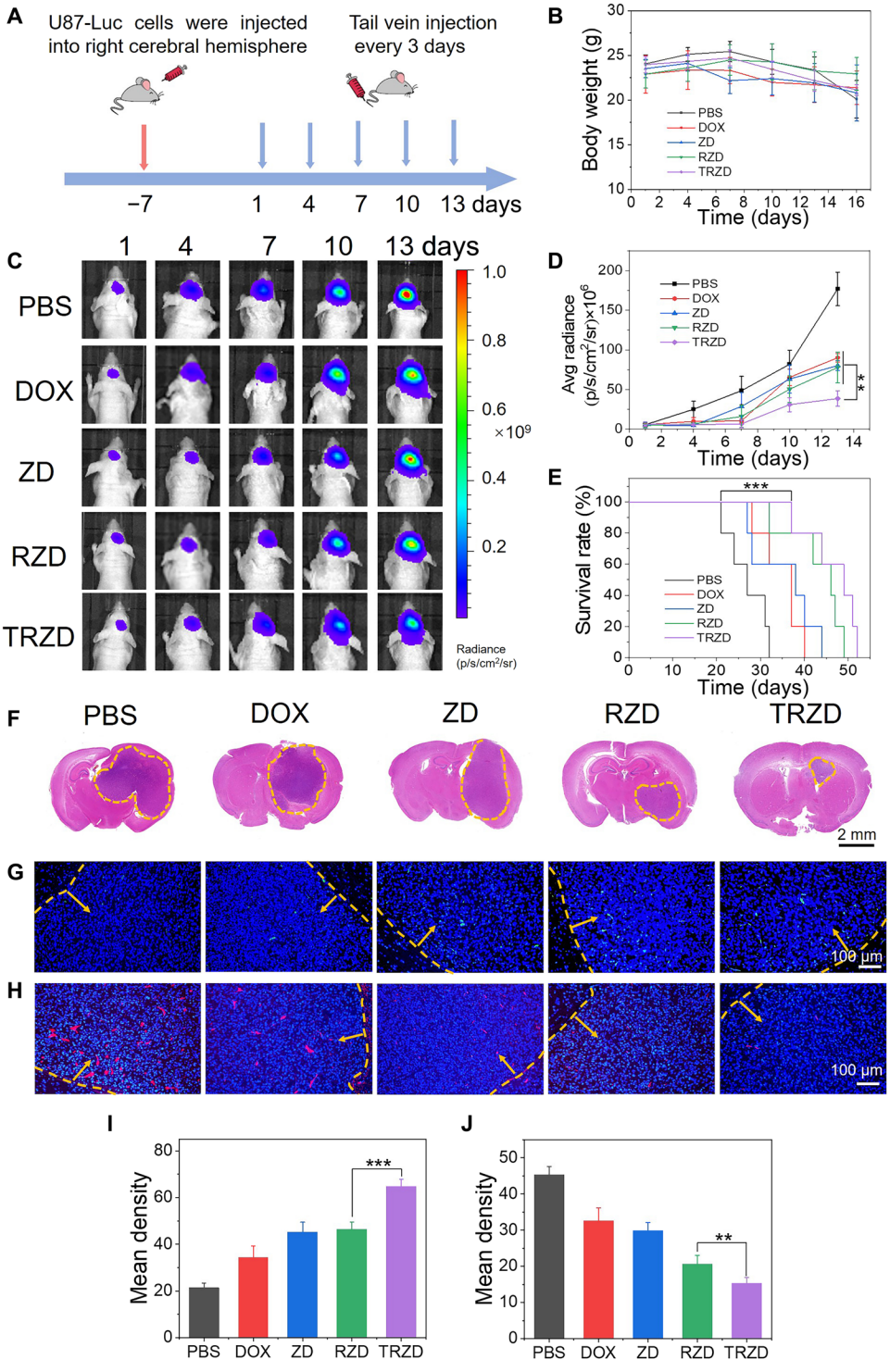

Fig. 8. In vivo study of the antitumor efficacy using an orthotropic cerebral glioma model. Mice with gliomas were administered with PBS, DOX, ZD, RZD, or TRZD. (**A**) Scheme of the experimental timeline. (**B**) Profiles of the change in the body weight of mice. Data are presented as means ± SD ($n = 6$). (**C**) Representative luminescent images of U87-Luc glioma-bearing mice in different groups. (**D**) Intensity of luminescence in brain tumors. Data are presented as means ± SD ($n = 6$); $^{**}P < 0.01$. (**E**) Cumulative survival study. (**F**) H&E staining of brain tissues of orthotopic glioma-bearing mice. The yellow dashed lines represented the boundaries of glioma. (**G**) TUNEL staining and (**H**) CD31 staining of brain tissues of orthotopic glioma-bearing mice. Cell nuclei were stained with DAPI (blue). The yellow dashed lines represented the boundaries of glioma, and the yellow arrows point to glioma. Scale bars, 100 μm. The mean fluorescence intensity of images of (**I**) TUNEL staining and (**J**) CD31 staining was calculated using ImageJ. Data are presented as means ± SD ($n = 5$); $^{**}P < 0.01$.

(labeled by C and marked by the white arrows). However, no organic lesions were found in the RZD or TRZD groups. The results confirmed that, as a BBTB penetrable NP with the properties of glioma targeting and prolonged circulation, TRZD highly reduced the side effects of the drug and could be a promising drug carrier for imaging and therapy of glioma as well as other brain diseases.

A biomimetic BBTB penetrable NIR PLNP for the diagnosis and treatment of glioma was developed. The luminescence of the NIR PLNPs could last longer than 7200 s and still hold appreciable intensity, and luminescence can also be renewed with UV light. With the coating of RBM and the conjugation of the T7 peptide, TRZ NPs exhibited significantly higher permeability to cross the BBTB in vitro. Furthermore, TRZ NPs had a good diagnostic ability for the orthotopic glioma at regions of both the cerebrum and cerebellum. The lifetime of the NIR PLNPs for the diagnosis of the orthotopic U87-MG tumor was 24 hours, and it was 30 hours for the subcutaneous tumor. With the loading of DOX, TRZD enhanced the cellular uptake of DOX. The apoptosis rate of TRZD on U87-MG cells was 3.27 times and 2.51 times of that of ZD and RZD, respectively. Moreover, TRZD NPs prolonged the survival time of the mice and showed superior tumor inhibition when applied in both subcutaneous and orthotropic glioma mouse models. These findings provide insights into the development of biomimetic BBTB penetrable NIR PL nanodrug carriers for precise diagnosis and therapy for not only glioma but also other brain-related diseases.

MATERIALS AND METHODS

Materials

T7-based peptide (T7-Cys, CHAIYPRH, 92.0%) was purchased from GenScript (Zhejiang, China). DSPE-PEG2000-MAL was provided by Ruixi Biological Technology Co. (Xi'an, China). DOX and the Bradford Protein Assay Kit were obtained from Solarbio Science & Technology Co. Ltd. (Beijing, China). CCK-8 was purchased from Dojindo (Kumamoto, Japan). Minimum essential medium (MEM), RPMI 1640 medium, penicillin-streptomycin, FBS, and trypsin-EDTA were obtained from Gibco (Waltham, MA, USA). Chloroform, ethanol, ammonium hydroxide, cetyltrimethylammonium bromide (CTAB), tetraethyl orthosilicate, and triethylamine were purchased from Sinopharm Chemical Reagent Co. Ltd. (Shanghai, China).

Cell lines

Cell lines were obtained from the National Infrastructure of Cell Line Resource.

Animals

Nude BABL/c mice were purchased from Shanghai Experimental Animal Center (Shanghai, China). All studies involving animals were approved by the Research Ethics Committee of the Hong Kong Baptist University.

RBM derivation

RBM was obtained according to a previously reported method with modification (*42*). Briefly, whole blood from the heart of the rat was collected and centrifuged at 1000*g* for 10 min at 4°C to collect RBC. Hemoglobin was removed by centrifugation (12,000*g*, 10 min, and 4°C). The collected RBM was stored at −20°C for subsequent studies.

Synthesis of MSNs

MSN was prepared according to the literature with modification (*43*). Briefly, DI water (560 ml), ethanol (160 ml), and ammonium hydroxide (1 ml) were mixed with CTAB (11.50 g) and stirred for 30 min. After further stirring in an oil bath for 30 min at 60°C, 30 ml of tetraethylorthosilicate was added into the mixture drop by drop, and the reaction was continued at 60°C for 2 hours and then cooled to 25°C. After centrifugation, the samples were washed with ethanol and DI water for three times, dried at 60°C for 12 hours, and annealed at 550°C for 5 hours to obtain MSN.

Synthesis of ZM

ZM was synthesized based on MSNs according to the literature with modification to limit the size distribution (*44*). One milliliter of Ga(NO3)3 solution (1 M) was mixed with Zn(CH3COO)2·2H2O, Cr(CH3COO)3, and $SnCl_4$ at an atomic ratio of Ga:Zn:Cr:Sn = 1.98:1:0.01:0.01 to form precursor solution, which was then mixed with 1 g of MSN and dried in a vacuum oven at 60°C for 12 hours. The dried sample was presintered at 600°C for 2 hours with a heating rate of 5°C/min. After grounding the heated mixture into powders, the presintered material was annealed at 1000°C for 4 hours. Last, ZM was obtained after cooling down to 25°C.

Preparation of RZ and TRZ

To prepare RZ, RBM with protein concentrations of 0.08, 0.2, 0.4, and 2 mg/ml was mixed with 1 mg of ZM and sonicated at 100 W for 10 min at 4°C. DSPE-PEG2000-MAL was conjugated to the cysteine residues of T7 to form DSPE-PEG2000-Mal-MAL. Briefly, T7 peptides were reacted with DSPE-PEG2000-Mal in a molar ratio of 1.5:1 in the solvent of the mixture of chloroform and triethylamine for 24 hours. The reactants were dialyzed with DI water for 48 hours to eliminate the organic solvent and the unreacted agents. Solutions in the dialysis bag were concentrated and dried using a rotary evaporator to obtain dry powders. Analysis using ^{1}H NMR and FTIR was carried out. To prepare T7-conjugated RZ (TRZ), the lipid insertion technique was used. DSPE-PEG2000-T7 was incubated with RZ in PBS (pH 7.4) for 4 hours to produce TRZ. To test the conjugation efficiency, a dye of the T7 peptide, TMR, was used and conjugated on T7 of TRZ. The conjugation efficiency of T7 was calculated according to the formula as follows

$$\text{Conjugation efficiency (\%)} = \frac{\text{Total T7} - \text{Free T7}}{\text{Total T7}} \times 100\%$$

Preparation of ZD, RZD, and TRZD

To prepare ZD, the solution of ZM was sonicated for complete dispersion. Then, DOX was added into the dispersion and stirred for 24 hours. After the reaction, DOX residual was removed by dialysis. Following a similar procedure, RZD and TRZD were prepared by loading DOX into RZ and TRZ. EE of DOX was determined using spectrophotometric methods. Drug LE and EE were calculated according to the formulas as follows

$$\text{Drug loading efficiency (\%)} = \frac{\text{Weight of the DOX encapsulated}}{\text{Weight of the nanoparticles}} \times 100\%$$

Encapsulation effciency (%) =

$$\frac{\text{Weight of the DOX encapsulated}}{\text{Weight of the total DOX added}} \times 100\%$$

The respective in vitro DOX release profiles of free DOX, ZD, RZD, and TRZD were obtained using the dialysis method. A DOX equivalent concentration of 1 mg/ml and dialysis bags with a cutting off molecular weight of 10 kDa were selected for the tests. Dialysis bags containing the prepared solutions of free DOX, ZD, RZD, and TRZD were kept in 25 ml of PBS (pH 7.4) under horizontal shaking at 100 rpm for 48 hours. At selected time points, 200 μl of the samples was collected and replaced with 200 μl of fresh PBS. The amounts of the released DOX were measured using a microplate reader (Infinite F200, TECAN, Austria).

In vitro cell viability

U87-MG and U87-Luc cells were cultured in MEM medium and RPMI 1640 medium, respectively. The in vitro cytotoxicity of DOX, ZM, ZD, RZD, and TRZD was evaluated using CCK-8. U87-MG cells (1×10^4 cells per well) were separately cultivated into 96-well plates and incubated with DOX, ZM, ZD, RZD, and TRZD for 24 and 48 hours. At 1 hour, color intensity was recorded by measuring the absorbance of the cells at 450 nm.

Confocal laser scanning microscope studies

Cellular uptakes of U87-MG cells were examined using a confocal laser scanning microscope (CLSM; FV3000, Japan). Cells (3×10^4) were cultured for 2 days. Then, cells were treated with DOX, ZD, RZD, or TRZD for 2 hours. Cells were fixed with 4% formaldehyde for 30 min and washed with PBS again. The cell nucleus was stained with DAPI, and cellular uptake was observed using CLSM.

Apoptosis assay

The rate of apoptosis in U87-MG cells after incubating with DOX, ZD, RZD, or TRZD was evaluated using an annexin V–FITC/propidium iodide (PI) apoptosis detection kit (Beyotime, China). U87-MG cells (1×10^5) were cultured in a six-well plate and incubated at 37°C for 24 hours. Then, cells were treated with fresh culture medium containing DOX, ZD, RZD, or TRZD with a DOX equivalent concentration of 5 μg/ml. After 24 hours of incubation, cells were collected and stained, and then analyzed using flow cytometry.

Permeability through the in vitro BBB

bEnd.3 cells (5.0×10^4 cells per well) were seeded in a 24-well Transwell plate to establish the in vitro BBB model. After the cells were cultured at 37°C with 5% CO_2 for 7 days, TEER values of the cells, which indicated the tightness of the cell monolayer, were measured using the EVOM2 Epithelial Voltohmmeter (WPI, USA). The monolayer of the cells with at least 180 ohm·cm^2 of TEER was selected for further experiments. ZM, RZ, and TRZ were added to the apical chamber of the Transwell. After the cells were incubated for another 4 hours, the medium in the apical chamber was removed and the chamber was washed by PBS three times. Then, the luminescence of the apical and basolateral chambers was measured using IVIS.

In vivo imaging and biodistribution

For in vivo imaging, 200-μl suspensions of ZM, RZ, and TRZ with a ZM equivalent concentration of 2 mg/ml were excited by 254-nm UV light for 5 min and then suspensions were injected into the mice through their tail veins. UV light (254 nm), which has a strong bactericidal effect, is routinely used for surface sterilization. Long-term repeated exposures of UV light can induce skin cancer and cause great damage to the eyes. Careful protection should be provided when using 254-nm UV for diagnosis purposes. IVIS was used to obtain the fluorescent distribution of NPs in the whole mice at 0, 15, and 45 min. Ex vivo imaging of major organs was obtained after the mice were sacrificed.

Pharmacokinetics

Sprague-Dawley rats (220 to 230 g) were randomly divided into four groups ($n = 3$). DOX, ZD, RZD, or TRZD was administered intravenously via the tail vein with a DOX equivalent concentration of 5 mg/kg. At 0.25, 0.5, 1, 2, 4, 6, 12, 24, and 48 hours, blood samples were collected. The concentrations of DOX in the plasma were determined using high-performance liquid chromatography.

In vivo NIR PL imaging and evaluation of the antitumor activity using a subcutaneous U87 tumor model

The suspension of U87-MG cells (200 μl, 1×10^7 cells/ml) was subcutaneously injected into the mice. Mice were sacrificed 14 days after the injection, and subcutaneous tumors were cut into small pieces in the size of 4 mm^3. Pieces of tumor tissues were then subcutaneously placed into the right hind limb of nude mice. Seven days after the implantation, 200-μl suspensions of ZM, RZ, or TRZ with a ZM equivalent concentration of 2 mg/ml were excited by 254-nm UV light for 5 min and injected into mice through their tail veins for in vivo PL imaging. The mice were anesthetized and imaged using IVIS at 0, 0.5, 1, 2, 6, 8, 24, 36, and 48 hours. NPs with PL were re-excited by UV light for 5 min before imaging was taken at 2, 6, 8, 24, 36, and 48 hours. The exposure time of imaging was set as 60 s.

For antitumor activity, the mice were randomly divided into five groups ($n = 10$) and treated with saline, DOX, ZD, RZD, or TRZD with a DOX equivalent concentration of 5 mg/kg every 3 days. During the experiments, the body weight of the mice and the size of the tumors were recorded. Tumor volumes were calculated using the formula

$$\text{Tumor volume} = \frac{\text{Length} \times \text{Width}^2}{2}$$

In vivo NIR PL imaging using the orthotropic U87 glioma models

To establish cerebral and cerebellar glioma models, 6- to 8-week-old male nude mice (about 18 g) were obtained. U87 MG-Luc cells (5×10^5) were suspended in 3 μl of culture medium. For the cerebral glioma model, cell suspension was injected into the right cerebral hemisphere (0.4 mm anterior and 2 mm lateral to the bregma with 3 mm depth). For the cerebellar glioma model, cell suspension was injected into the right cerebellum (1 mm to the right of the midline and 1 mm posterior to the lambdoid suture with 3 mm depth). Ten days after injections, nude mice were imaged using IVIS for the confirmation of the successful establishment of the glioma model. On the next day, 200-μl suspensions of ZM, RZ, and TRZ with a ZM equivalent concentration of 2 mg/ml were excited for 5 min using UV light and injected into the mice through their tail veins for the in vivo PL imaging. The mice were anesthetized and imaged using IVIS at 5, 15, and 30 min, and 2, 4, 8, and 24 hours. NPs with PL

were re-excited by UV light for 5 min before the imaging was taken at 2, 4, 8, and 24 hours. The exposure time of imaging was set as 60 s.

Evaluation of the antitumor activity using an orthotropic U87 glioma model

For the evaluation of the antitumor activity, mice of the orthotropic U87 cerebral glioma model were randomly divided into five groups ($n = 6$). From day 0, each group of mice was intravenously injected with 200 μl of PBS, DOX, ZD, RZD, or TRZD with a DOX equivalent concentration of 5 mg/kg every 3 days. During the experiments, the body weight of the mice and the imaging of the tumors were recorded.

Immunofluorescence histochemical analysis

Tumors of the subcutaneous U87 tumor model and brain tissues of the orthotropic U87 glioma model were separately fixed with 4.0% paraformaldehyde. TUNEL staining and CD31 staining were applied on the paraffin-embedded tissue sections. Fluorescence images of each tissue section were obtained and analyzed by ImageJ.

Statistical analysis

All experimental results were expressed as means ± SD. The significance of group differences for normally distributed data was assessed by one-way analysis of variance (ANOVA) followed by Tukey's test. $P < 0.05$ was considered statistically significant. In vivo images were collected using IVIS, and fluorescence and luminescence intensities were statistically analyzed using the IVIS software. The other data were analyzed using the Origin 8.1 software.

SUPPLEMENTARY MATERIALS

Supplementary material for this article is available at https://science.org/doi/10.1126/sciadv.abm7077

View/request a protocol for this paper from *Bio-protocol*.

REFERENCE AND NOTES

1. W. Li, L. Ren, X. Zheng, J. Liu, J. Wang, T. Ji, G. Du, 3-O-Acetyl-11-keto-β-boswellic acid ameliorated aberrant metabolic landscape and inhibited autophagy in glioblastoma. *Acta Pharm. Sin. B* **10**, 301–312 (2020).
2. Y. Jia, X. Wang, D. Hu, P. Wang, Q. Liu, X. Zhang, J. Jiang, X. Liu, Z. Sheng, B. Liu, H. Zheng, Phototheranostics: Active targeting of orthotopic glioma using biomimetic proteolipid nanoparticles. *ACS Nano* **13**, 386–398 (2019).
3. C. Wang, B. Wu, Y. Wu, X. Song, S. Zhang, Z. Liu, Camouflaging nanoparticles with brain metastatic tumor cell membranes: A new strategy to traverse blood-brain barrier for imaging and therapy of brain tumors. *Adv. Funct. Mater.* **30**, 1909369 (2020).
4. G. Grahovac, D. Tomac, S. Lambasa, A. Zoric, M. Habek, Cerebellar glioblastomas: Pathophysiology, clinical presentation and management. *Acta Neurochir.* **151**, 653–657 (2009).
5. R. Babu, R. Sharma, I. O. Karikari, T. R. Owens, A. H. Friedman, C. Adamson, Outcome and prognostic factors in adult cerebellar glioblastoma. *J. Clin. Neurosci.* **20**, 1117–1121 (2013).
6. D. W. Townsend, Multimodality imaging of structure and function. *Phys. Med. Biol.* **53**, R1–R39 (2008).
7. T. Maldiney, B. T. Doan, D. Alloyeau, M. Bessodes, D. Scherman, C. Richard, Gadolinium-doped persistent nanophosphors as versatile tool for multimodal in vivo imaging. *Adv. Funct. Mater.* **25**, 331–338 (2015).
8. D. Ma, X. Chen, Y. Wang, Q. Guo, Q. Ye, R. Guo, S. Xiao, Q. Ye, Y. Huang, Y. Peng, Benzyl ester dendrimer silicon phthalocyanine based polymeric nanoparticle for in vitro photodynamic therapy of glioma. *J. Lumin.* **207**, 597–601 (2019).
9. J. Tang, N. Huang, X. Zhang, T. Zhou, Y. Tan, J. Pi, L. Pi, S. Cheng, H. Zheng, Y. Cheng, Aptamer-conjugated PEGylated quantum dots targeting epidermal growth factor receptor variant III for fluorescence imaging of glioma. *Int. J. Nanomed.* **12**, 3899–3911 (2017).
10. Q. L. M. de Chermont, C. Chanéac, J. Seguin, F. Pellé, S. Maîtrejean, J.-P. Jolivet, D. Gourier, M. Bessodes, D. Scherman, Nanoprobes with near-infrared persistent luminescence for in vivo imaging. *Proc. Natl. Acad. Sci. U.S.A.* **104**, 9266–9271 (2007).
11. R. Weissleder, V. Ntziachristos, Shedding light onto live molecular targets. *Nat. Med.* **9**, 123–128 (2003).
12. A. M. Smith, M. C. Mancini, S. Nie, Bioimaging: Second window for in vivo imaging. *Nat. Nanotechnol.* **4**, 710–711 (2009).
13. A. J. Tavares, L. Chong, E. Petryayeva, W. R. Algar, U. J. Krull, Quantum dots as contrast agents for in vivo tumor imaging: Progress and issues. *Anal. Bioanal. Chem.* **399**, 2331–2342 (2011).
14. T. Maldiney, A. Bessière, J. Seguin, E. Teston, S. K. Sharma, B. Viana, A. J. Bos, P. Dorenbos, M. Bessodes, D. Gourier, D. Scherman, C. Richard, The in vivo activation of persistent nanophosphors for optical imaging of vascularization, tumours and grafted cells. *Nat. Mater.* **13**, 418–426 (2014).
15. A. Nonat, C. F. Chan, T. Liu, C. Platas-Iglesias, Z. Liu, W.-T. Wong, W.-K. Wong, K.-L. Wong, L. J. Charbonnière, Room temperature molecular up conversion in solution. *Nat. Commun.* **7**, 11978 (2016).
16. H. Zhao, C. Liu, Z. Gu, L. Dong, F. Li, C. Yao, D. Yang, Persistent luminescent nanoparticles containing hydrogels for targeted, sustained, and autofluorescence-free tumor metastasis imaging. *Nano Lett.* **20**, 252–260 (2020).
17. H. Zhao, G. Shu, J. Zhu, Y. Fu, D. Yang, Persistent luminescent metal-organic frameworks with long-lasting near infrared emission for tumor site activated imaging and drug delivery. *Biomaterials* **217**, 119332 (2019).
18. L. X. Yan, L. J. Chen, X. Zhao, X. P. Yan, pH switchable nanoplatform for in vivo persistent luminescence imaging and precise photothermal therapy of bacterial infection. *Adv. Funct. Mater.* **30**, 1909042 (2020).
19. K. Chen, Y. Wang, H. Liang, S. Xia, W. Liang, J. Kong, Y. Liang, X. Chen, M. Mao, Z. Chen, X. Bai, J. Zhang, J. Li, Y.-n. Chang, J. Li, G. Xing, Intrinsic biotaxi solution based on blood cell membrane cloaking enables fullerenol thrombolysis in vivo. *ACS Appl. Mater. Interfaces* **12**, 14958–14970 (2020).
20. J. Xu, Y. Zhang, J. Xu, G. Liu, C. Di, X. Zhao, X. Li, Y. Li, N. Pang, C. Yang, Y. Li, B. Li, Z. Lu, M. Wang, K. Dai, R. Yan, S. Li, G. Nie, Engineered nanoplatelets for targeted delivery of plasminogen activators to reverse thrombus in multiple mouse thrombosis models. *Adv. Mater.* **32**, 1905145 (2020).
21. J. Ma, S. Zhang, J. Liu, F. Liu, F. Du, M. Li, A. T. Chen, Y. Bao, H. W. Suh, J. Avery, G. Deng, Y. Zhou, P. Wu, K. Sheth, H. Wang, J. Zhou, Targeted drug delivery to stroke via chemotactic recruitment of nanoparticles coated with membrane of engineered neural stem cells. *Small* **15**, 1902011 (2019).
22. H. Wu, X. Jiang, Y. Li, Y. Zhou, T. Zhang, P. Zhi, J. Gao, Engineering stem cell derived biomimetic vesicles for versatility and effective targeted delivery. *Adv. Funct. Mater.* **30**, 2006169 (2020).
23. L. Rao, G.-T. Yu, Q.-F. Meng, L.-L. Bu, R. Tian, L.-S. Lin, H. Deng, W. Yang, M. Zan, J. Ding, A. Li, H. Xiao, Z.-J. Sun, W. Liu, X. Chen, Cancer cell membrane-coated nanoparticles for personalized therapy in patient-derived xenograft models. *Adv. Funct. Mater.* **29**, 1905671 (2019).
24. X. Zhen, P. Cheng, K. Pu, Recent advances in cell membrane–camouflaged nanoparticles for cancer phototherapy. *Small* **15**, 1804105 (2019).
25. Y. Duan, M. Wu, D. Hu, Y. Pan, F. Hu, X. Liu, N. Thakor, W. H. Ng, X. Liu, Z. Sheng, H. Zheng, B. Liu, Biomimetic nanocomposites cloaked with bioorthogonally labeled glioblastoma cell membrane for targeted multimodal imaging of brain tumors. *Adv. Funct. Mater.* **30**, 2004346 (2020).
26. L. Cai, C. Yang, W. Jia, Y. Liu, R. Xie, T. Lei, Z. Yang, X. He, R. Tong, H. Gao, Endo/lysosome-escapable delivery depot for improving BBB transcytosis and neuron targeted therapy of Alzheimer's disease. *Adv. Funct. Mater.* **30**, 1909999 (2020).
27. Y. Z. Zhao, B. X. Shen, X. Z. Li, M. Q. Tong, P. P. Xue, R. Chen, Q. Yao, B. Chen, J. Xiao, H. L. Xu, Tumor cellular membrane camouflaged liposomes as a non-invasive vehicle for genes: Specific targeting toward homologous gliomas and traversing the blood–brain barrier. *Nanoscale* **12**, 15473–15494 (2020).
28. C. P. Foley, D. G. Rubin, A. Santillan, D. Sondhi, J. P. Dyke, Y. Pierre Gobin, R. G. Crystal, D. J. Ballon, Intra-arterial delivery of AAV vectors to the mouse brain after mannitol mediated blood brain barrier disruption. *J. Control. Release* **196**, 71–78 (2014).
29. C. T. Curley, N. D. Sheybani, T. N. Bullock, R. J. Price, Focused ultrasound immunotherapy for central nervous system pathologies: Challenges and opportunities. *Theranostics* **7**, 3608–3623 (2017).
30. R. M. Jones, L. Deng, K. Leung, D. M. Mahon, M. A. O'Reilly, K. Hynynen, Three-dimensional transcranial microbubble imaging for guiding volumetric ultrasound-mediated blood-brain barrier opening. *Theranostics* **8**, 2909–2926 (2018).
31. A. Jana, P. Narula, A. Chugh, R. Kulshreshtha, Efficient delivery of anti-miR-210 using Tachyplesin, a cell penetrating peptide, for glioblastoma treatment. *Int. J. Pharm.* **572**, 118789 (2019).
32. B. S. Varnamkhasti, S. Jafari, F. Taghavi, L. Alaei, Z. Izadi, A. Lotfabadi, M. Dehghanian, M. Jaymand, H. Derakhshankhah, A. A. Saboury, Cell-penetrating peptides: As a promising theranostics strategy to circumvent the blood-brain barrier for CNS diseases. *Curr. Drug Deliv.* **17**, 375–386 (2020).
33. K. B. Johnsen, A. Burkhart, L. B. Thomsen, T. L. Andresen, T. Moos, Targeting the transferrin receptor for brain drug delivery. *Prog. Neurobiol.* **181**, 101665 (2019).

34. A. K. Kondapi, Targeting cancer with lactoferrin nanoparticles: Recent advances. *Nanomedicine* **15**, 2071–2083 (2020).
35. N. Kuplennik, K. Lang, R. Steinfeld, A. Sosnik, Folate receptor α-modified nanoparticles for targeting of the central nervous system. *ACS Appl. Mater. Interfaces* **11**, 39633–39647 (2019).
36. Q. Guo, Q. Zhu, T. Miao, J. Tao, X. Ju, Z. Sun, H. Li, G. Xu, H. Chen, L. Han, LRP1-upregulated nanoparticles for efficiently conquering the blood-brain barrier and targetedly suppressing multifocal and infiltrative brain metastases. *J. Control. Release* **303**, 117–129 (2019).
37. Y. Anraku, H. Kuwahara, Y. Fukusato, A. Mizoguchi, T. Ishii, K. Nitta, Y. Matsumoto, K. Toh, K. Miyata, S. Uchida, K. Nishina, K. Osada, K. Itaka, N. Nishiyama, H. Mizusawa, T. Yamasoba, T. Yokota, K. Kataoka, Glycaemic control boosts glucosylated nanocarrier crossing the BBB into the brain. *Nat. Commun.* **8**, 1001 (2017).
38. M. Allix, S. Chenu, E. Véron, T. Poumeyrol, E. A. Kouadri-Boudjelthia, S. Alahraché, F. Porcher, D. Massiot, F. Fayon, Considerable improvement of long-persistent luminescence in germanium and tin substituted $ZnGa_2O_4$. *Chem. Mater.* **25**, 1600–1606 (2013).
39. A. Bessière, S. Jacquart, K. Priolkar, A. Lecointre, B. Viana, D. Gourier, $ZnGa_2O_4$: Cr^{3+}: A new red long-lasting phosphor with high brightness. *Opt. Express* **19**, 10131–10137 (2011).
40. L. You, J. Wang, T. Liu, Y. Zhang, X. Han, T. Wang, S. Guo, T. Dong, J. Xu, G. J. Anderson, Q. Liu, Y.-Z. Chang, X. Lou, G. Nie, Targeted brain delivery of rabies virus glycoprotein 29-modified deferoxamine-loaded nanoparticles reverses functional deficits in parkinsonian mice. *ACS Nano* **12**, 4123–4139 (2018).
41. P. Zhang, L. Hu, Q. Yin, Z. Zhang, L. Feng, Y. Li, Transferrin-conjugated polyphosphoester hybrid micelle loading paclitaxel for brain-targeting delivery: Synthesis, preparation and in vivo evaluation. *J. Control. Release* **159**, 429–434 (2012).
42. Z. Chai, D. Ran, L. Lu, C. Zhan, H. Ruan, X. Hu, C. Xie, K. Jiang, J. Li, J. Zhou, J. Wang, Y. Zhang, R. H. Fang, L. Zhang, W. Lu, Ligand-modified cell membrane enables the targeted delivery of drug nanocrystals to glioma. *ACS Nano* **13**, 5591–5601 (2019).
43. Z.-A. Qiao, L. Zhang, M. Guo, Y. Liu, Q. Huo, Synthesis of mesoporous silica nanoparticles via controlled hydrolysis and condensation of silicon alkoxide. *Chem. Mater.* **21**, 3823–3829 (2009).
44. R. Zou, S. Gong, J. Shi, J. Jiao, K.-L. Wong, H. Zhang, J. Wang, Q. Su, Magnetic-NIR persistent luminescent dual-modal ZGOCS@ MSNs@Gd_2O_3 core–shell nanoprobes for in vivo imaging. *Chem. Mater.* **29**, 3938–3946 (2017).

Acknowledgments

Funding: This work is financially supported by the General Research Fund of Hong Kong (15304119 to G.-L.L. and Y.W. and 15334316 and 12302921 to Y.W.), the Health and Medical Research Fund of the Food and Health Bureau of Hong Kong (05161016 and 07183026 to Y.W.), and the Environmental and Conservation Fund of the Environment Protection Department of Hong Kong (2020-48 to Y.W.). **Author contributions:** Y.W. conceived the idea and designed the experiments. J.K. and R.Z. performed the experiments. J.K. and G.-L.L. analyzed the data. G.-L.L. provided suggestions on the research. Y.W. and J.K. wrote the paper. All authors contributed to the general discussion. **Competing interests:** The authors declare that they have no competing interests. **Data and materials availability:** All data needed to evaluate the conclusions in the paper are present in the paper and/or the Supplementary Materials.

Submitted 6 October 2021
Accepted 14 January 2022
Published 9 March 2022
10.1126/sciadv.abm7077

ScienceAdvances

Biomimetic multifunctional persistent luminescence nanoprobes for long-term near-infrared imaging and therapy of cerebral and cerebellar gliomas

Jianglong KongRui ZouGa-Lai LawYi Wang

Sci. Adv., 8 (10), eabm7077. • DOI: 10.1126/sciadv.abm7077

Science Advances (ISSN) is published by the American Association for the Advancement of Science. 1200 New York Avenue NW, Washington, DC 20005. The title *Science Advances* is a registered trademark of AAAS.